Experimental Validation of a Rigorous Absorber Model for CO_2 Postcombustion Capture

Finn Andrew Tobiesen and Hallvard F. Svendsen
Dept. of Chemical Engineering, Norwegian University of Science and Technology, NTNU, NO-7491 Trondheim, Norway

Olav Juliussen
Dept. of Chemical Engineering, SINTEF Materials and Chemistry, NO-7465 Trondheim, Norway

DOI 10.1002/aic.11133
Published online March 2, 2007 in Wiley InterScience (www.interscience.wiley.com).

A rigorous rate-based model for acid gas absorption was developed and validated against mass-transfer data obtained from a 3-month campaign in a laboratory pilot-plant absorber in which the experimental gas–liquid material balance was within an average of 6%. The mass-transfer model is based on the penetration theory where the liquid film is discretized using an adaptive grid. The model was validated against all data and the deviation between simulated and averaged gas and liquid side experimental mass-transfer rates yielded a total variability of 6.26%, while the total average deviation was 6.16%. Simpler enhancement factor mass-transfer models were also tested, but showed slight over-prediction of mass-transfer rates. A sensitivity analysis shows that the accuracy of the equilibrium model is the single most important source of deviation between experiments and model, in particular at high loadings. Experimental data for the absorber in the integrated pilot plant are included. © 2007 American Institute of Chemical Engineers *AIChE J,* 53: 846–865, 2007

Keywords: CO_2 absorption, absorber model, experimental validation, laboratory pilot plant, MEA

Introduction

Inherent advantages of fossil fuels, such as availability, relatively low cost, and the existing infrastructure for delivery and distribution, make them likely to play a major role in the world energy production at least for the next 50 years to come. Combustion of coal and natural gas are main sources of CO_2 emissions, which according to the Intergovernmental Panel on Climate Change (IPCC) constitute the major man-made contribution to global warming.[1] This has led to a number of measures around the world to address this problem. The most viable and commercially available CO_2 capture technology today is based on postcombustion CO_2 absorption.[2,3] In this process CO_2 is captured from the flue gases after the conversion of fuel into power. Typically, the CO_2 concentrations are 3–5% in natural gas-fired and 13–15% in coal-fired power plants. To properly understand the mechanisms associated with this removal technology, for accurate plant design, and for process improvement, precise modeling of the whole absorption/desorption process is crucial.

Specific system description

The process studied in this article is a conventional amine absorption process, as described in Tobiesen et al.[4] Although several commercial process packages for sour-gas absorption exist, e.g. Aspen Plus, Hysys, Protreat,

Correspondence concerning this article should be addressed to F. A. Tobiesen at andrew.tobiesen@sintef.no.

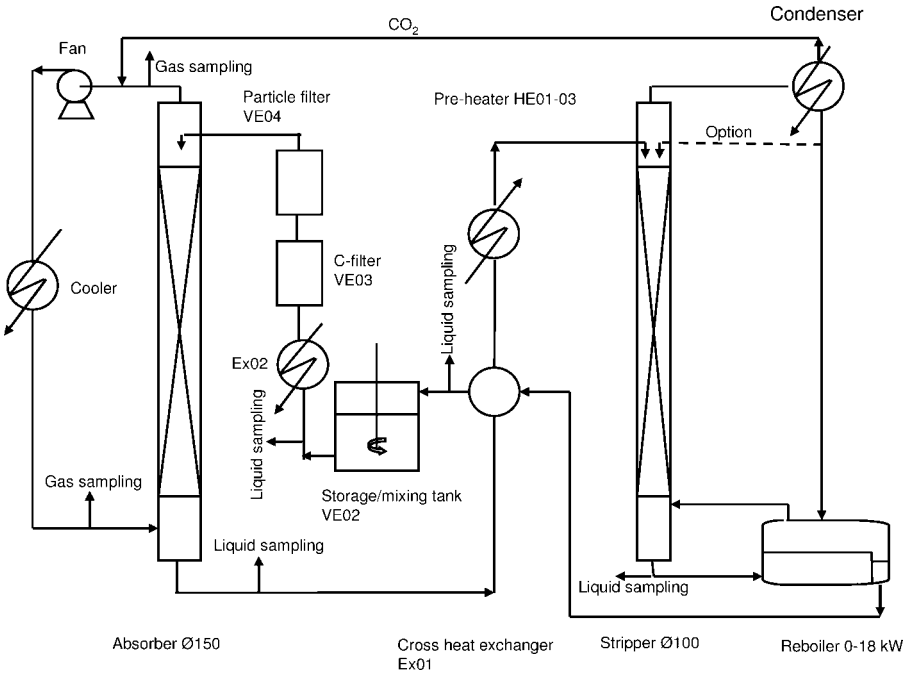

Figure 1. Simplified flow sheet of the laboratory pilot plant.

Tsweet, these are limited as to the number of absorbent systems that are included. At the same time, there are few models describing the absorption process published in the open literature. Commercial software packages are based on different methods for the tower calculations, such as stage-wise or rate-based approaches. It is commonly accepted that a rate-based approach has a potential for the most accurate description of the absorber and desorber behavior. A schematic diagram of the apparatus used in this work, similar to an industrial amine absorption process, is shown in Figure 1.

The rate based methodology for simulating a packed-column laboratory absorber was early presented by Danckwerts and Alper.[5] De Leye and Froment[6] modeled isothermal chemical gas absorption, while Pandya[7] performed packed-column absorber simulations for amine and potash solutions. More recently, Alatiqi et al.[8] developed a rate-based model for absorbers and desorbers using a mixing-cell approach and an enhancement factor model for the effect of chemical reaction. Kucka et al.[9] and Al-Baghli et al.[10] developed rate-based models for absorption with MEA and DEA, respectively, using approximations and numerical solutions for the film model, respectively, for describing mass transfer. Recently, Freguia and Rochelle[11] modeled a basic absorption flowsheet with MEA using a rate-based interfacial mass-transfer model assuming a pseudo first-order reaction. However, significant discrepancies between the models are observed, and only few are supported with experimental verification.

The objective of this work is to validate the absorber part of a rigorous rate-based simulation program for a complete absorption/desorption process, using detailed data from a pilot plant available in our laboratories. The model is implemented in FORTRAN 90. The mass-transfer model is developed based on the penetration theory with special emphasis on implementing numerical techniques that give accurate and rapid convergence. Simpler and faster interfacial models based on enhancement factors are also implemented and evaluated. Emphasis has been put on easy adaptation of the code to different absorbent systems. All subprograms use standardized syntax and the unit operations are modularized to facilitate changes in flow-sheet configuration and equilibrium and mass-transfer model.

The developed model is based on data and correlations from the open literature and from separate experiments in own laboratories, e.g. chemical equilibria. No fitting to experimental results from the pilot rig were done, and the model and the pilot-plant experimental data are independent of each other in their entirety. This article concentrates on the validation of the absorber section and a subsequent paper will focus on the desorber section of the pilot rig. The developed model is written primarily for modeling CO_2 removal from postcombustion flue gas systems at atmospheric pressure, but can equally well be used for modeling acid gas absorption from natural gas or other process streams, e.g. blast furnace gases.

Model and Model Implementation

Flow model

The general flow model, see Appendix A, is based on the assumption of plug flow of both gas and liquid. Implementation of an axial dispersion model was considered, and can easily be realized, but all correlations for mass-transfer coefficients and contact area found in the open literature are based on the plug-flow assumption and would need re-evaluation in order to be used with an axial dispersion model. The

plug-flow concept is deemed to be reasonable at low gas densities and reasonable velocities (<2–3 m/s). However, for demanding applications at higher pressures and gas and liquid loads, it may be questionable. Also for very high recovery values of acid gas (>95–99%), there will be significant sensitivity for backmixing effects.

Gas/liquid interfacial model

Several interfacial flux models are implemented in the overall contactor model. A rigorous penetration theory-based model, see Appendix B, is implemented using numerical routines aimed particularly at cases with large interfacial concentration gradients. A schematic concentration and temperature profile for a transferring component represented by a separate liquid and gas section is shown in Figure 2. The adaptive grid used for solving the transport equations is also described in Appendix B. The driving force for absorption is expressed in terms of activities for all the mass-transfer models. This is a more accurate way of expressing driving forces and is easily implemented since nonidealities are explicitly accounted for and calculated in the thermodynamic equilibrium model.

Analytical solutions for interfacial mass transfer with chemical reaction are restricted to asymptotic cases in which simplified assumptions about the reaction regimes are made. It is generally accepted that for absorption within the fast pseudo first-order reaction regime, i.e. $3 < Ha$ and $E_\infty > 5Ha$, the enhancement factor can be expressed as the Hatta number:

$$E = Ha = \frac{\sqrt{D_{CO_2} k_{ov} C_{MEA}}}{k_{CO_2 L}} \tag{1}$$

This asymptotic approximation is in general valid when the concentration of free MEA (C_{MEA}) does not change much throughout the reaction zone.

The enhancement model formulated by DeCoursey for reversible second-order reactions (first order with respect to CO_2)[12] is given as:

$$E_{Dec} = \frac{-Ha^2}{2(E_\infty - 1)} + \left[\frac{Ha^4}{4(E_\infty - 1)^2} + \frac{E_\infty Ha^2}{(E_\infty - 1)} + 1\right]^{\frac{1}{2}} \tag{2}$$

where the enhancement factor for an instantaneous equilibrium chemical reaction between CO_2 and MEA can be expressed as:[13,14]

$$E_\infty = 1 + \frac{\frac{D_{MEACOO^-}}{D_{CO_2}} \sqrt{K_{Eq,CO_2} C_{MEA}}}{\left[\left(1 + 2\frac{D_{MEACOO^-}}{D_{MEA}}\right)\sqrt{K_{Eq,CO_2} C_{CO_2,free,b}}\left(\sqrt{C_{CO_2,free,b}} + \sqrt{C_{CO_2,free,in}}\right)\right]} \tag{3}$$

K_{Eq,CO_2} is the equilibrium constant for the reaction as defined by Weiland et al.[14] The interfacial concentration of CO_2 enters into this equation making the solution iterative.

The DeCoursey model assumes that the diffusivities of all components are equal and the expression covers a larger reaction region than the pseudo first-order assumption by using so-called "bridging relations" between the reactant concentrations.

One of the more recent enhancement models is the one expressed by Hogendoorn et al.,[15] the Secor–Beutler–DeCoursey (SBDC) model. Based on the equation given by DeCoursey,[12] it also requires iteration to obtain concentrations of amine and CO_2 at the interface.

The interfacial sensible heat transfer is modeled using a simple heat-transfer coefficient approach where the heat-transfer coefficient is deduced from the mass-transfer coefficient and the Chilton–Colburn analogy.[16]

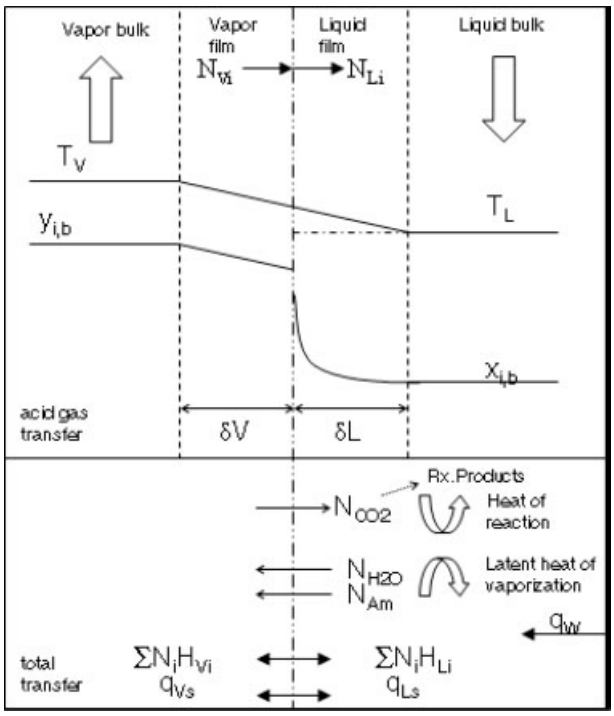

Figure 2. Interfacial mass transfer for a differential element in the packing.

Use of molar flows and enthalpy flows

To ensure consistency throughout the different subroutines, the flows are standardized to molar flows. The program therefore uses molar fluxes, mole fractions, and molar enthalpy flows. This is favorable since the changes in volumetric properties do not have to be accounted for in the system while being solved, e.g., values on concentration basis can easily be obtained from molar fractions by having an expression for the density as a function of component molar fractions and liquid temperature. This is needed for determining several hydraulic properties for the tower and can be calculated at any point in the program.

The use of enthalpy flows instead of fluid temperature is preferred because a large concentration of bound CO_2 is present in the liquid phase during absorption, causing the liquid heat capacity to change considerably. By consistently using the component specific enthalpy instead of temperature, one will account for the liquid phase heat capacity for the mixture (including chemically bound CO_2) while only using the liquid heat capacity for the unloaded solution as primary measured data, see equations in Appendix D. This approach relies on accurate values for the CO_2 heat of absorption and liquid-phase enthalpies, since these are used explicitly as basis for the change in liquid-phase enthalpy.

Numerical scheme

The mathematical problem arising from the resulting steady-state absorber model is a two-point boundary value problem (BVP) in a single dimension which needs to be discretized. Basic algorithms required to solve these problems include the finite difference types and the collocation types. In this work, the latter method has been chosen. The collocation methods have been frequently used in chemical engineering applications since adapted by Villadsen and Michelsen.[17] Other methods were also tested but the comparisons are not addressed here. The collocation method is of a spectral type and is inherently more accurate than the finite difference types. They are always multipoint methods applying all points within the element to estimate the corresponding derivatives at the grid points. The finite difference method, in its simplest case, uses only neighboring grid points to estimate derivatives at the grid point.

While simultaneously solving the differential equations for mass and energy in the packing, it is not critical as to the path the numerical routines use toward convergence. However, the initial guesses should be realistic and further give physically meaningful values throughout the path to convergence. As already mentioned, the interfacial mass-transfer models used in this work are coded as stand-alone models. Therefore, also during the solution scheme of the column, a sequential strategy has been used. Along the path toward convergence, the mass-transfer model is solved to yield a flux for each transferring component at each grid point in the packing. The packing is then solved by the collocation routine.

Since the interfacial mass-transfer model yields equations that are highly nonlinear, an analytical expression for the derivatives is not obtainable. The interfacial flux model is called to obtain numerical approximations of the derivatives, in this case by finite differencing, in order to evaluate the Jacobian at each point. Consequently, the mass-transfer models must be solved a large number of times as the bulk phase mass and energy balances are solved. The number of calls to the mass-transfer models depends on the stiffness of the outer system of ordinary differential equations that represent the packing and also on the number of components that undergo phase transfer. The stiffer the system, the more collocation points per subinterval is needed, which requires a larger number of grid points. The computational load will therefore depend mainly on the rate of convergence of the interfacial mass-transfer model, the number of times it has to be solved in order to solve the global packing segment, and the total number of times the thermodynamic package is called. The first and the last point can be significantly reduced by minimizing the number of discretization points in the liquid film. Since very large gradients occur at the interface, a large number of gridpoints is needed here, while less is needed towards the bulk. Large computational savings can therefore be realized by using adaptive grids when compared with fixed homogenous grids.

Vapor–liquid equilibrium

The speciation in the liquid phase, including the activity coefficient determinations for CO_2 and MEA, was calculated using an activity coefficient model as described by Hoff et al.[18,19] In the present model, however, the activity coefficient for CO_2 was not assigned to the Henry's law constant, but used to calculate CO_2 activity. The model was tuned to fit own experimental VLE data and data by Ma'mun et al.[20] The fit is shown in Figure 3. For the sensitivity analysis the model was also tuned to data of Jou et al.,[21] also shown in Figure 3. The thermodynamic model covers a temperature range from 40 to 125°C and CO_2 loadings up to 0.6 mole CO_2/mole MEA. The model fitting was performed using Marquardt's method with an in-house Matlab software package. The speciation plot for this system was compared with the one from Liu et al.[22] who used the NRTL model, similar to Austgen et al.,[23] but with refitted important parameters. The difference between their and our speciation plot is small. The speciation was also compared with NMR data at 20°C, Poplsteinova et al.,[24] and found to agree well. The accuracy of the equilibrium data as well as the model fitting is of crucial importance and a sensitivity analysis has been performed as described later.

Estimation of hydraulic properties

The penetration model requires an estimate of the average gas/liquid contact time between mixing points. The contact time could be obtained by considering the liquid load and liquid hold-up in the packing and estimating a distance between mixing points. In this work, however, we have used the correlation given by Rocha et al.[25,26] The same liquid side mass-transfer coefficient correlation was used in the enhancement factor-based models to ensure consistency between the penetration and enhancement factor models.

The correlation for effective interfacial area was obtained from De Brito et al.[27] and the correlations for liquid holdup and limits for flooding were obtained from Suess and Spiegel[28] and Billet and Schultes,[29] respectively. In Appendix C are given the models used for hydraulics, mass transfer, and physical properties. Since the interfacial area correlations found in the literature show significant variations, an evaluation and discussion is included.

Experimental Section

Description of the laboratory pilot plant

A simplified flow sheet for the pilot rig is shown in Figure 1 where also the sampling points are given. This is an integrated pilot plant operating with an absorber and desorber and connected unit operations. The absorber input conditions were therefore determined by the overall plant operation and

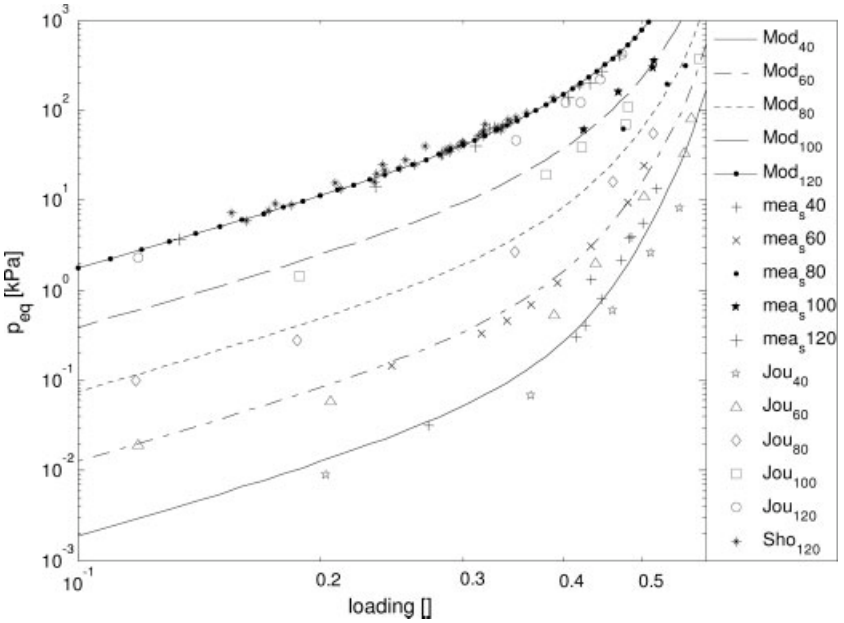

Figure 3. Experimental data and equilibrium model.

the operating conditions of no two runs were identical. Stability tests were performed by maintaining one steady state for about 15 h and sampling liquid and gas in three campaigns at intervals of about 5 h. Examples are Runs 2–4 in Tables E1 and E2. The pilot plant can process about 150 N m^3/h of gas with CO_2 contents between 0.3 and 25 vol %. The capture capacity is about 10 kg CO_2/h from gas containing 3% CO_2, depending on liquid loading. The data presented in this work were obtained during continuous operation over a period of 3 months. The system is fully automated and files of logged data were recorded continuously during operation. Data for the pilot absorber unit and operating conditions can be found in Table 1.

Several parameters were changed during this period to accomplish a broad spectrum of operational conditions. Data for absorption and stripping were recorded simultaneously but only the absorber data are reported here. The height of packing is such that the whole operating range for an industrial contactor cannot be achieved in one experiment, but rather for a section of the tower. However, the tests were run such that the whole operating range for a normal absorber was studied. The tests were performed with 30 wt % MEA. At the beginning of the measurements, the lower range of the loading interval was studied, and after build up of CO_2 loading, the higher loading ranges were tested until the upper loading range was reached. It was convenient to divide the operation into three loading ranges, covering the complete loading spectrum for MEA. These were defined as ranges 1–3 being 0.20–0.30, 0.30–0.40, and 0.40–0.45, respectively. Liquid sample points are given in Figure 1, and liquid species concentrations and solvent densities were obtained. At least 2–3 parallel sampling operations were performed for each steady state. In addition the pressure and liquid temperature were measured in and out of the absorber plus the temperature profile inside the column.

In Appendix E, Tables E1 and E2 are included as a complete set of measured data for inlet and outlet gas and liquid streams to the absorber packing for all 20 runs. The experimental temperature profiles are only included for four runs shown graphically. The full set of temperature profile data can be obtained from the authors upon request.

Analyses

Before liquid sampling, about 100–200 ml of liquid was withdrawn. Then a sampling bottle was filled totally with about 50 ml of sample, closed tightly, cooled and analysed within 48 h. The CO_2 concentrations were determined using the $BaCl_2$ method and the amine concentrations were determined by titration as described by Ma'mun et al.[20] The gas was sampled directly from the return gas pipeline about 20 cm above the top of the absorber, cooled to about 10°C, and sent to an IR analyzer (Rosemount Binos 100). The amounts of condensate formed during cooling were very small in all runs. They were analyzed for amine and the concentrations were very low. The CO_2 analyzers were calibrated by using calibrated mass flow controllers for CO_2 and nitrogen. Calibration was performed after each run, with at least 4–5 different concentrations covering the whole range of interest.

Table 1. Packing Parameters and Operation Conditions for the Absorber

Asorber Characteristics	
Column internal diameter (m)	0.15
Main Packing height (m)	4.36
Packing	Sulzer Mellapak 250Y
Parameter	
Liquid circulation rate (l/s)	3–9
MEA concentration (wt%)	30.0
Rich solution loading (kmol/kmol)	0.267–0.451
Lean solution loading (kmol/kmol)	0.183–0.410
Temperature lean stream to absorber (°C)	40–66
Temperature rich stream out of absorber (°C)	41–69
Absorber pressure (kPa)	99–104

Table 2. Sensitivity Analysis: Overal CO_2 Mass Transfer Rates Obtained in Absober Column for Experimental Data as well as Simulation data

Simulation	Exp Liq/Gas Mass Flow Deviation	Base Case Simulator	1	2	3	4	5	6	7	8	9
AAD (%)	4.43	6.24	9.97	9.17	9.04	6.11	6.17	6.05	5.89	6.19	10.79
AD (%)	5.68	6.16	10.06	8.96	8.99	5.88	6.21	6.13	6.30	6.16	11.78

Pecrcentage deviation: x_i.

AAD-absolute average deviation defined as: $\frac{1}{n}\sum_{i=1}^{n}|x_i - \bar{x}|$.

AD-average deviation: $\frac{1}{n}\sum_{i=1}^{n}|x_i|$ where $x_i = \frac{v_{sim} - v_{ex}}{v_{ex}} \times 100$.

All calibrated temperature probes (PT-100 resistance temperature sensors) were calibrated to a precision of about $\pm 0.1^{\circ}C$ with a Beamex calibrator.

Each time liquid samples were withdrawn from the system for analyses, operational data were obtained by averaging over a 30-min interval around the sampling time. After a change in operational conditions the plant was run for at least 5 h to ensure steady state operation.

Liquid density and CO_2 concentrations were measured for the absorber inlet and outlet. The amine concentration was only measured at the absorber inlet and the outlet concentration was assumed to be the same. Along the absorber, five temperature measurements were made for each run. Together with the inlet and outlet liquid and gas temperatures, these yielded a total of nine temperatures for the column profiles. It was not possible to determine whether the temperature probes within the column measured liquid or gas phase. The temperature plots for the two phases therefore use the same internal temperatures, while the gas and liquid temperatures at the ends were added to the set.

The gas from the absorber together with reclaimed CO_2 from the stripper were recycled back to the absorber inlet. The carrier gas mainly consisted of nitrogen and water vapor. The two lines to the CO_2 analyzer were placed just after the absorber exit and before the absorber inlet respectively. It was assumed that the gas exiting the absorber was saturated with water and amine at the upper packing temperature. The partial pressure of H_2O, $p(T_{l,in})^{W}_{H_2O}$, at the top of the column, was obtained using a Wilson correlation[30] where the parameters were taken from Nath and Bender.[31] The wet basis CO_2 partial pressure was then obtained as described by Ma'mun et al.[20] The absorber feed was assumed saturated with water at the measured inlet temperature and the water content obtained by using steam table data.[32]

Individual liquid and gas phase mass balances for CO_2 could be obtained based on the content of CO_2 in both phases. The accuracy of the balances was assumed to be about the same. When comparing the results with the simulations, an average of the two was therefore used to determine the CO_2 mass transfer in the column.

Results and Discussion

Base model for absorber validation

The simulation model was tested against all the obtained experimental data, which included 20 data acquisition periods during the continuous pilot-rig operation. The following experimental data were used as basis for the absorber model validation:

- Incoming liquid and gas streams to the absorber: molar flow rate, F; component molar fraction of liquid and gas phase, x_i and y_i; temperature and pressure, T, p.
- The outlet liquid and gas streams from the absorber: molar flow rate, F; component molar fraction, x_i and y_i; temperature and pressure, T, p.
- Five temperatures through the absorber packing to yield a temperature profile.

A base-case model was defined for the initial validation. As base-case interfacial mass-transfer model the penetration model was used with 31 adaptive gridpoints. The overall reaction-rate expression was obtained from Versteeg et al.,[33] while heat of reaction was obtained from Mathonat et al.[34] and supplemented with own data. The various correlations used in the model can be found in Appendix C.

Evaluation and accuracy of the experimental data

A material balance around the absorber requires that the CO_2 absorbed by the solvent should equal the CO_2 removed from the gas. Table 2 shows that there is a 4.43% absolute average deviation (AAD) between these two for the experimental data, whereas the absolute deviation (AD) is 5.58%. This indicates a systematic deviation in the data as the liquid phase measurements on average show about 1.1% lower mass transfer than the gas phase measurements. This systematic deviation is so small that it is acceptable and actually can be taken as a support for the quality of the experimental data. The mass-transfer rates from gas and liquid analyses are compared in Figure 4. The figure shows that the deviations are larger in the highest loading range and the small systematic deviation between gas and liquid side is also visible. The largest errors that affect the experimental results are expected to stem from errors in gas phase CO_2 calibrations and errors in analyzing CO_2 in the solvent. The expected uncertainty in the gas phase CO_2 measurements is $\pm 2\%$ and similar for the liquid phase. This is in good agreement with the differences and AADs found. In the higher loading interval there can be some CO_2 lost from the MEA due to flashing when sampling and this will yield a too low measured loading. However, the sampling procedure has been checked for much higher loadings than obtained during the pilot experiments, and this effect is thought to be negligible. A

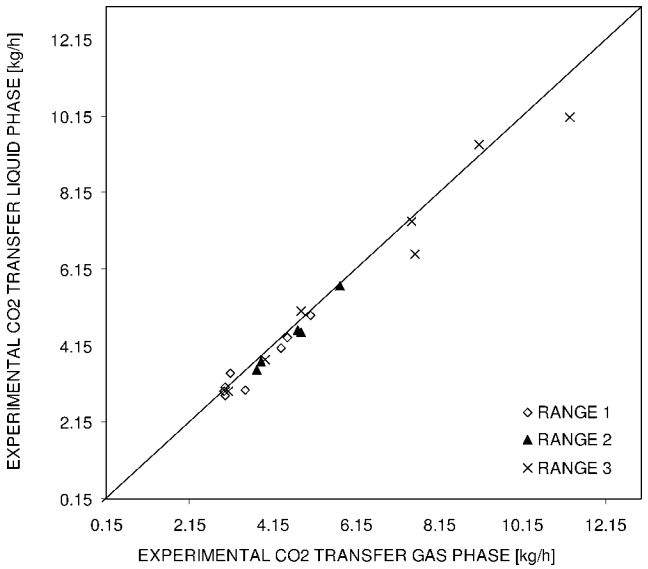

Figure 4. Experimental mass-transfer rates (kg/h), calculated based on the gas and liquid phase.

Loading range 1: rich loading <0.3; loading range 2: rich loading >0.3 and <0.4; loading range 3: rich loading >0.4.

significant error can occur if the estimation of water vapor in the inlet gas stream is erroneous. As mentioned, it is assumed that the inlet gas, being piped back from the absorber outlet, is at its saturation pressure over pure water. If the inlet partial pressure were assumed to be at equilibrium with the amine solution in the absorber sump at the measured inlet temperature, and calculated according to a Wilson equation, this would decrease its value and adversely affect the simulated temperature curves in the packing. The inlet molar content of CO_2 gas would also change about 1–2% since the CO_2 gas content is measured on dry basis.

Comparison between experiments and base case model

CO_2 absorption rates. The experimental CO_2 loading of the rich solution leaving the column and the corresponding values predicted by the model can be found in Table 3 for all 20 runs. As seen from the table, the agreement is very good. However, comparing experimental and simulated outlet loading is not a good measure for the model accuracy. The sensitivity to errors is low and data shown in this fashion may conceal significant discrepancies. It is necessary to compare the experimental and simulated amounts of CO_2 transferred. Figure 5 shows experimental and simulated mass-transfer rates for all 20 runs. The experimental mass-transfer rates are averages of the gas and liquid phase measurements. The first thing to be noted is that the scatter in the data is larger than when comparing loading values. This indicates that mass-transfer rate is a much more sensitive measure when comparing experiments and simulations. In spite the scatter, the agreement between experiments and simulated values is deemed satisfactory throughout the whole loading range. It is particularly noteworthy that the experiments at high loading, but with low mass-transfer rates, do not stand out with large deviations. With high loading and low mass transfer the liquid phase analyses are difficult as one obtains the mass transfer by subtracting two large numbers. However, some increased scatter is observed for the results in this range.

The mass-transfer trends shown by the simulation model are very reasonable. The total variability (AAD), see Table 3, of the experimental average gas and liquid side mass-transfer rates compared with the simulated mass-transfer rates for the complete data set is 6.24%, while the total AD

Table 3. Experimental Data and Simulated Results for Individual Experimental Runs, Part 1

		Rich Loading			Outlet pCO_2		Absorbed CO_2		
Run*	Lean Loading, Exp	Exp	Sim	Inlet pCO_2 (kPa)	Exp (kPa)	Sim (kPa)	Exp Avg (kg/h)	Sim (kg/h)	% dev Abs CO_2,x_i**
1	0.218	0.284	0.276	1.603	0.377	0.431	3.27	2.96	−0.60
2	0.220	0.275	0.274	1.513	0.332	0.405	2.93	2.79	−4.78
3	0.215	0.272	0.269	1.509	0.343	0.406	2.98	2.80	−5.84
4	0.217	0.276	0.272	1.513	0.333	0.403	3.04	2.81	−7.55
5	0.216	0.274	0.283	1.779	0.339	0.367	3.24	3.41	−5.31
6	0.183	0.267	0.267	2.148	0.297	0.354	4.43	4.34	−1.92
7	0.284	0.345	0.351	2.727	0.756	0.711	4.66	4.90	5.28
8	0.241	0.296	0.299	2.205	0.413	0.426	4.22	4.30	1.70
9	0.233	0.299	0.302	2.631	0.523	0.496	5.01	5.10	1.75
10	0.217	0.333	0.333	2.477	0.539	0.615	4.66	4.53	−2.66
11	0.219	0.309	0.310	1.917	0.384	0.480	3.64	3.51	−3.64
12	0.307	0.401	0.403	2.686	1.133	1.134	3.79	3.79	0.09
13	0.297	0.390	0.400	5.429	2.305	1.974	7.43	8.09	8.98
14	0.370	0.433	0.455	4.001	2.792	2.600	3.02	3.40	12.70
15	0.357	0.435	0.443	10.299	6.355	5.611	9.25	10.30	11.28
16	0.402	0.447	0.458	8.228	6.626	6.103	3.88	4.62	18.96
17	0.409	0.451	0.449	12.112	9.964	9.868	4.94	4.65	−5.91
18	0.346	0.429	0.426	9.841	5.058	5.637	10.70	9.69	−5.91
19	0.347	0.400	0.404	6.683	3.310	3.512	7.05	6.85	−2.87
20	0.292	0.339	0.338	3.716	1.143	1.182	5.75	5.57	−3.12

*Sorted by date.
**$x_i = \frac{v_{sim} - v_{ex}}{v_{ex}} \times 100$.

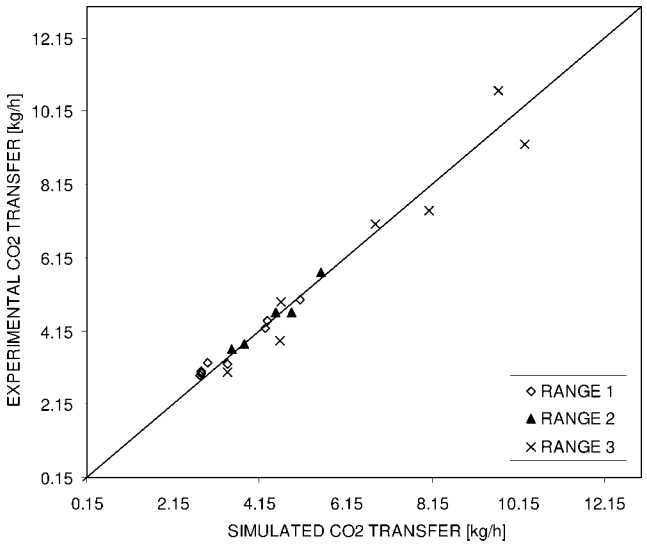

Figure 5. Comparison of experimental and simulated mass-transfer rates (kg/h).

Loading range 1: rich loading <0.3; loading range 2: rich loading >0.3 and <0.4; loading range 3: rich loading >0.4.

is 6.16%. This shows that the agreement between simulated and experimental results is good and that there is no systematic deviation to be found. The relative deviation between simulated and experimental absorption rate for single runs varies between 19% and −9.6% and the overall agreement is deemed to be satisfactory.

Comparison of simulated and experimental temperature profiles. The experimental results for the gas and liquid temperatures in and out plus the temperature profiles for four sets of data compared with the simulated ones are shown in Table 4 and in Figures 6–9. These cases were chosen because they cover almost the whole experimental loading range for MEA.

The difference between inlet and outlet liquid temperature in the experiments, as seen from Table 4, varies between about 7–8°C for the low loading range, with highest CO_2 up-takes, to about 4–5°C for the highest loading range where the CO_2 up-take is the lowest. Table 4 also shows the simulated outlet liquid temperatures and the correspondence between experimental and simulated values is good. Because of the recycle of gas, the difference between inlet and outlet gas temperatures is somewhat smaller, ranging from 2 to 5°C. Also here the accordance between experimental and simulated values is reasonable. This trend is further supported by the experimental and simulated temperature profiles in Figures 6–9. There seems to be a slight under-prediction of the heat evolved in the experiments with low loading, whereas a small over-prediction can be seen for loading range 3 (rich loading >0.40). This is in spite the fact that the absorption rate predictions are equally good over the whole loading range as noted earlier. However, the amount of CO_2 absorbed only partly explains and determines the temperature profiles. The temperature curves are also strongly dependent on the amount of condensation and evaporation of water and amine in the packing, and thereby on the estimates made for water content in the inlet and outlet gas. These water contents were not measured during the pilot tests. A relatively small change in the estimated water concentrations change the inlet vapor composition and yield significant changes in the simulated temperature profiles. In particular, good estimates for the inlet gas water content are important for the temperature profiles. As noted under the discussion of experimental errors, a shift in inlet water content will affect the experimental results as it enters into the mass balance calculation for CO_2. In addition, it will enter into the driving force and temperature calculations in the model. It was found that changing the water content in the inlet gas from a value

Table 4. Experimental Data and Simulated Results for Individual Experimental Runs, Part 2

	Liquid Temp °C			Vapor Temp °C		
Run*	Exp Inlet**	Exp Outlet**	Sim Outlet	Exp Inlet**	Exp Outlet	Sim Outlet
1	40	41	40.4	39	42.2	42.7
2	41	42	41.3	40	41.9	43.5
3	40	41	40.3	39	41.3	42.5
4	41	42	41.3	40	41.7	43.5
5	51	55	54.9	54	53.4	54.7
6	50	56	55.0	54	55.6	54.8
7	49	53	53.3	52	53.4	52.7
8	48	52	51.5	50	52**	51.0
9	61	64	63.0	62	64.7	63.9
10	48	56	54.9	54	58**	54.8
11	48	54	53.8	53	55.8	53.5
12	46	52	51.8	51	54.4	51.9
13	60	66	65.0	64	68.4	65.8
14	48	52	51.7	51	53.8	52.8
15	59	64	63.5	62	66.6	64.5
16	61	61	60.8	60	62.9	63.5
17	66	67	68.8	68	68.5	68.6
18	62	69	69.9	69	72.4	67.9
19	64	68	67.3	66	70.5	67.4
20	64	67	65.5	64	68.8	66.2

*Sorted by date.
**Only measured to whole degress (°C).

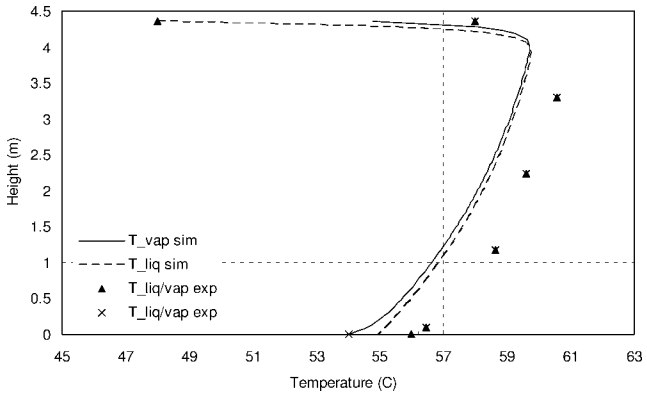

Figure 6. Comparison between experimental and simulated temperature profile for loading range 1, Run 10: Change in loading (lean-rich): experiment: 0.217–0.333, simulated: 0.217–0.333.

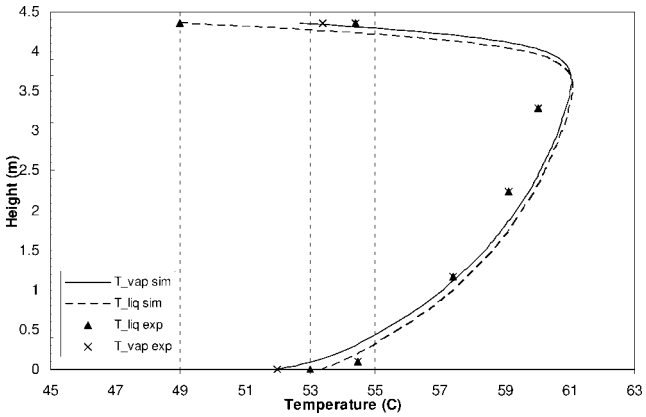

Figure 8. Comparison between experimental and simulated temperature profile for loading range 2, Run 12: Change in loading (lean-rich): experiment: 0.307–0.400, simulated: 0.307–0.403.

being in equilibrium with the amine solution at the inlet temperature, to being in equilibrium with pure water at the same temperature, would shift the simulated temperature profiles by 1–3°C. Thus, the discrepancies that are shown between experimental and simulated temperature profiles may well stem from errors in estimating the water vapor content in the inlet gas stream.

The temperature profiles in most of the runs show the typical absorption bulge toward the top of the absorber. The size of this bulge has to do with the degree of CO_2 absorption whereas the location of the bulge has to do with the g/l ratio and the amine and CO_2 available for absorption at a given packing height. The experimental temperature bulge increases were 8–25% for our runs. Freguia and Rochelle report from 15 to 35% for an industrial absorber operation.[11] The smaller temperature bulges reported here have to do with the lower loading difference in our absorption experiments and thus less absorption with a higher relative circulation rate. The varying CO_2 content into the column (3–15%) makes a direct comparison difficult. The location of the bulge is almost entirely in the upper part of the packing, indicating that most of the absorption occurs here. This is reasonable since the ratio of amine to CO_2 is quite low. This is also in accordance with the findings of Dugas et al.[35]

If the liquid/gas rate is increased or the packing height lowered, the bulge will appear more to the center of the packing. Also the inlet water content affects the position of the temperature bulge as a low content will tend to pull the bulge downwards in the column.

Code efficiency at gas/liquid interface and liquid film. Figure 10 shows concentration profiles for various species in the liquid film at the top of the absorber for Run 10 (loading range 1) and at the bottom of the absorber for Run 15 (loading range 3). The amine species are normalized with the total bulk amine concentration while the gas phase components are normalized with the bulk gas-phase concentrations. Run 10 has a loading at the top of the packing of 0.22 and a gas phase CO_2 content of 0.62 vol %, while Run

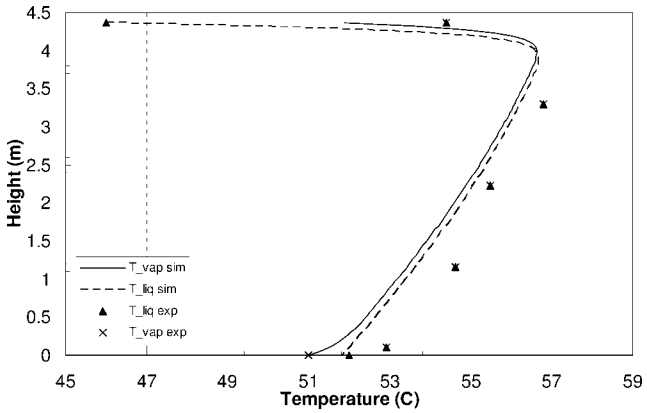

Figure 7. Comparison between experimental and simulated temperature profile loading range between 1 and 2, Run 7: Change in loading (lean-rich): experiment: 0.284–0.345, simulated: 0.284–0.351.

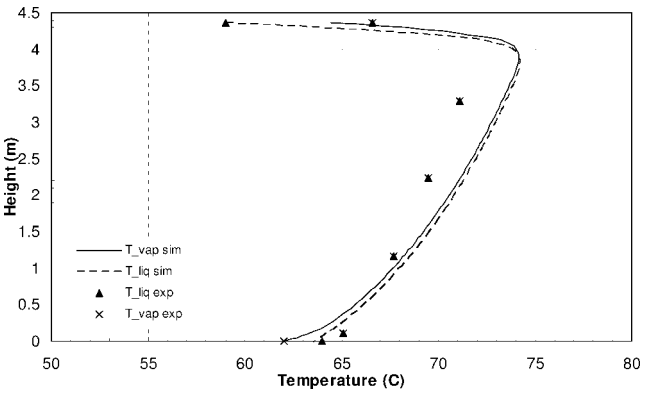

Figure 9. Comparison between experimental and simulated temperature profile for loading range 3, Run 15: Change in loading (lean-rich): experiment: 0.357–0.434, simulated: 0.357–0.442.

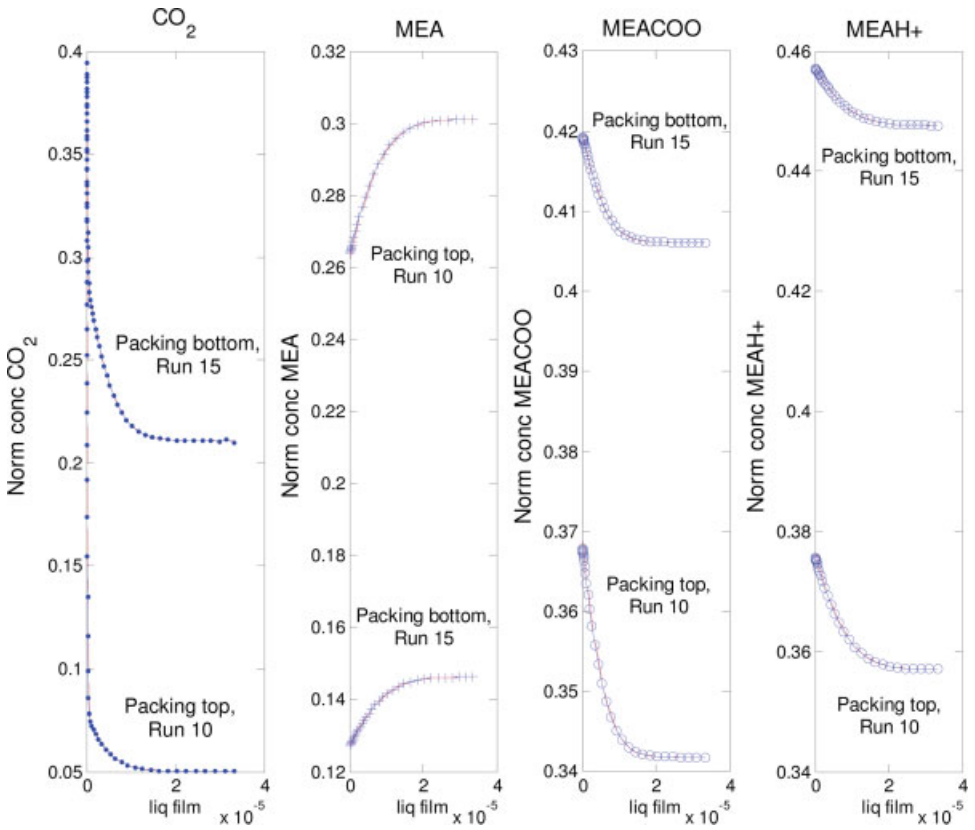

Figure 10. Normalized concentration profiles in liquid film at top and bottom of packing for loading range 1, Run 10 and range 3, Run 15, respectively.

[Color figure can be viewed in the online issue, which is available at www.interscience.wiley.com.]

15 has a rich loading of 0.44 and a corresponding CO_2 content of 9.98 vol %. These are two very different cases and it is essential that the code works sufficiently well, without changing any system parameters, for all possible cases that can occur. For the penetration model calculations, the adaptive grid proved very efficient. It was found that 31 grid points, with both absolute and relative tolerance set to 1E-6, one order of magnitude smaller than the outer packing model, were sufficient. This number of gridpoints was found to give less than 0.1% change in AD for the complete dataset compared with using 51 gridpoints. The bulk of these grid points are found very close to the gas liquid interface, as is best seen on the CO_2 graph. Note that it is necessary to choose a sufficient film thickness to ensure that all the components reach equilibrium at the bulk side of the film. However, it is not important if the chosen film depth is too large because of the adaptive nature of the grid. At the top inlet the reaction is extremely fast as can be seen from the depletion of CO_2 at the interface. Another interesting point that can be noted here is that the MEA concentrations vary significantly close to the interface, both for Run 10 at the top of the packing and for Run 15 at the bottom. At the bottom the depletion of the small amount of free MEA available in the film is quite large and therefore can give rise to a diffusion-controlled interfacial mass-transfer zone. This suggests that the first-order approximation implicit in some mass-transfer models may not be valid even in this case.

An investigation of the mass-transfer results as function of different liquid phase circulation rates showed no systematic deviations. The results thus indicate that the model describes the effect of liquid flow rate properly.

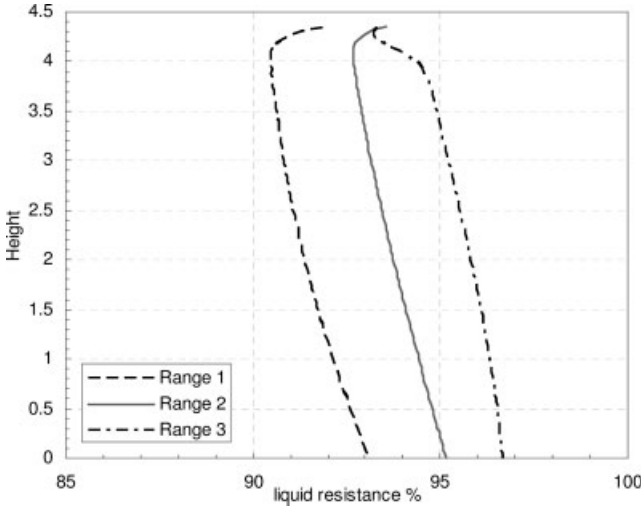

Figure 11. Liquid side mass-transfer resistance versus position in packing.

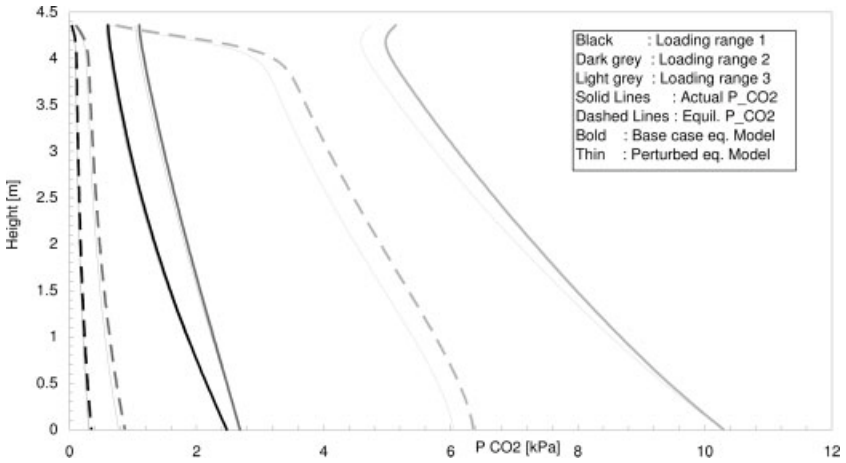

Figure 12. CO_2 partial pressures along packing. Simulations from Run 10 (Loading range 1: base sim: 0.217–0.334), Run 12 (Loading range 2: base sim: 0.307–0.407), Run 15 (Loading range 3, base sim: 0.357–0.441).

The role of liquid-film resistance. Chemical absorption is normally strongly influenced by liquid-film resistance. The fraction of the liquid-film resistance can be defined as follows:

$$\mathrm{res}_{\mathrm{L},\mathrm{CO}_2} = \frac{\frac{1}{\bar{k}_{\mathrm{CO}_2\mathrm{L}}}}{\frac{1}{\bar{k}_{\mathrm{CO}_2\mathrm{L}}} + \frac{1}{k_{\mathrm{CO}_2\mathrm{G}} H_{\mathrm{CO}_2}}} \tag{4}$$

where $\bar{k}_{\mathrm{CO}_2\mathrm{L}}$ is the time-averaged liquid mass-transfer coefficient obtained from the numerical solution of the penetration model.

Figure 11 shows that the liquid-phase resistance steadily increases as loading increases, but in the pilot tests it varied only from about 87 to 97%. It can be concluded that the CO_2 mass-transfer resistance is located almost entirely on the liquid side, however, its contribution is reduced to below 90% in the more reactive sections of the column, e.g., at low loading at the top of the packing. These simulations represent relatively narrow loading regions and not the entire range expected in an industrial column. It may occur for industrial cases, notably at the top of the packing at low CO_2 partial pressures and low loadings, that the gas phase resistance becomes more dominant.

Model sensitivity

There are several possible sources of error in the model presented in this paper. The use of a penetration model should hopefully account for different reaction regimes occurring along the packing compared with more simplified models, such as, an asymptotic simplified solution using a pseudo first-order regime enhancement factor model, is likely to fail at the higher loadings, as the enhancement factor in this case may not be assumed equal to the Hatta number.

Regardless of interface model used, the reaction-rate estimate will normally become less accurate at higher temperatures, partially because of lack of data and because an Arrhenius exponential extrapolation might not always be accurate, as shown by Aboudheir et al.[36]

Even more important are the uncertainties associated with the equilibrium data and the equilibrium model. Finally, the lumped parameters describing penetration model contact time, the hydrodynamic properties of the packing, and in particular, the correlations used for the effective interfacial area are normally all found from empirical correlations based on experimental data from systems not necessarily representative for the absorption system in question. A parameter sensitivity analysis covering some of these parameters was therefore undertaken.

The importance of equilibrium model. The explicit thermodynamic model used in this work was fitted to equilibrium data obtained from in-house VLE experiments, shown in Figure 3. In Figure 12 are shown the gas CO_2 partial pressures (solid lines) compared with the liquid-phase equilibrium partial pressures (dashed lines) for Runs 10, 12, and 15. In Figure 13 the same data are converted to driving forces along the packing. The solid lines show results for the base-case equilibrium model and represent the three loading ranges.

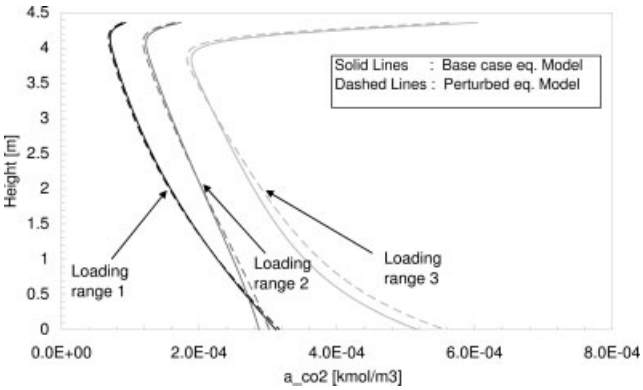

Figure 13. Driving forces for CO_2 along packing. Simulations from Run 10 (Loading range 1: base sim: 0.217–0.334), Run 12 (Loading range 2: base sim: 0.307–0.407), Run 15 (Loading range 3, base sim: 0.357–0.441).

For all simulations, regardless of loading range, the driving force, seen from the tower top, starts with a high value, decreases rapidly, and then increases toward the bottom of the absorber. The sharp decrease at the tower top is caused by the rapid increase in temperature, seen in Figures 6–9, and reflected by the sharp increase in equilibrium partial pressure in this region, shown in Figure 12. In the rest of the tower, the driving forces increase due to the increase in gas phase CO_2 partial pressure, whereas the equilibrium partial pressure has a smaller effect. This is caused by the way the experiments were set up as one tried to follow an operating line of an industrial column, thereby increasing the CO_2 partial pressure with increasing loading.

In Figures 12 and 13 are also shown curves for the driving force profiles for a small perturbation of the equilibrium model, thin lines in Figure 12, and the dashed lines in Figure 13. The DeCoursey enhancement factor model was used for the example. The equilibrium curves for CO_2 were moved 0.01 loading units to the left. This corresponds to a change of 2–4% in loading value which is of the same magnitude as the actual accuracy in the loading determinations. The total MEA concentration was left unchanged but the free MEA concentrations will change slightly because of this shift in loading. The negative shift in loading reduces backpressure and as can be seen in the high loading range in Figure 12, even such a small perturbation of the equilibrium data results in a higher CO_2 up-take and a significant reduction in the actual partial pressures in the tower. In Figure 13 this is converted to driving forces and it is clear that this change in the equilibrium curve has only a small effect at the lower loading regimes. This is caused by the near parallel shift in actual gas phase and equilibrium partial pressure. In loading range 3 the difference in driving forces are larger since the backpressure is lower at the bottom of the absorber.

Figures 12 and 13, however, only show changes in driving forces. A change in the equilibrium model will also affect the mass-transfer rate calculations. In Figure 14 are shown the overall liquid side-based mass-transfer coefficients. These are defined as the ratio between the mass-transfer rates, and the driving forces given in Figure 13. The solid lines represent the simulations with the base case equilibrium model. It can be seen that the largest mass-transfer coefficients occur where the column temperature is at its highest, just below the top. The general trend is that the mass-transfer coefficients have the opposite behavior of the driving forces. At high driving forces the mass-transfer coefficients are lowest, and highest for the low driving forces. They increase with temperature, being highest in the high temperature zones where the driving forces are at their minimum. This is expected as both reaction rates and diffusion coefficients increase with temperature.

In Figure 14 are also shown the effects of shift in equilibrium model on the mass-transfer coefficient, indicated by the dashed lines. This effect is shown to be visible, but relatively small for the low and medium loading ranges. However, for the high loading range the effect is stronger, with an increase of 10–15% as indicated by comparing the solid and dotted light grey lines. This is twice the effect compared with the lower loading ranges. This shows the sensitivity to the equilibrium model, and of course to the equilibrium data on which it is based, when calculating the mass-transfer fluxes

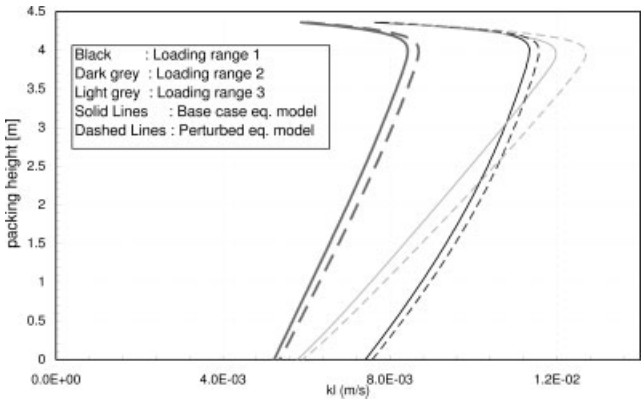

Figure 14. Overall liquid side-based mass-transfer coefficient versus packing height, loading ranges 1–3.

in the high loading ranges. This is believed to be a general observation for all amine systems.

In Table 5 are shown the individual mass-transfer coefficients for both the liquid and gas side. $\bar{k}_L$ is the contact time averaged liquid side mass-transfer coefficient based on liquid phase activity driving force. k_G is the gas side coefficient based on liquid side activity driving force, and k_G^o is the gas side coefficient based on gas phase concentration driving force. $H_{\infty,SOL}$ is the infinite dilution Henry's law constant.

In column 9 in Table 2 is shown the effect of the perturbation in the equilibrium model on the total data set. The AAD and the AD increase from 6.24 and 6.16%, respectively, to 10.7 and 11.78%.

Enhancement factor models. Since the numerical solution of the penetration model is quite time consuming when simulating an absorption column, it is a matter of significant practical importance to determine if a simpler interfacial model can be used.

Figure 15 shows plots of the obtained enhancement factors using the three enhancement factor models tested plus enhancement factors calculated based on the penetration model. The results from loading range 1 show that the enhancement factors obtained from the DeCoursey and SBDC models are very close to the penetration model results whereas the simple Hatta number model shows significant deviation even at the low loadings. In loading range 2 the discrepancies between the models become clearer. The DeCoursey and SBDC models are very close together, the Hatta number model yields higher enhancement factors, and all three are very optimistic compared with the penetration model. In loading range 3 the differences between the models become very large. The Hatta number model in this case predicts enhancement factors nearly twice as large as the penetration model. The DeCoursey and SBDC models are very similar, but about 50% higher than the penetration model predictions. In Figure 16 are shown the deviations between predicted mass-transfer rates and experimental ones from the models when used on the pilot plant tests. The results are given in ascending loading order which is not the same as the run number order. It is clear that all models give about the same result up to a rich loading of about 0.35–0.40. Compared with the differences just found in the enhancement factor

Table 5. Individual Mass Transfer Coefficients in Liquid and Gas side for Runs 10 and 15

Packing Height (m)*	K_L (10^{-3}, m/s)	k_L^{-1} $(m/s)^{-1}$	k_G^{-1} $(m/s)^{-1}$	k_G^{o-1} $(m/s)^{-1}$	$H_{\infty,\,SOL}$ [kPa/(kmol/m^3)]
Run 10					
4.36	7.69	119.4	10.58	22.01	5671.6
4.011	11.3	79.99	8.452	21.18	6934.7
3.008	10.7	84.51	8.578	21.33	6868.2
2.006	9.84	92.82	8.786	21.54	6751.4
1.003	8.69	106	9.083	21.81	6583.0
0	7.28	127.8	9.498	22.19	6354.6
Run 15					
4.36	7.64	122.2	8.787	21.28	6797.4
4.011	8.78	107.4	6.522	18.87	8350.8
3.008	7.19	132.4	6.686	19.23	8273.1
2.006	5.98	160.2	7.036	20.00	8124.3
1.003	4.92	195.6	7.514	20.41	7696.9
0	4.03	239.8	8.313	21.74	7287.6

*Postion from bottom,

$K_L^{-1} = k_L^{-1} + k_G^{-1}, \quad k_G = \left(\frac{k_G^o}{R_g T_g} H_{\infty,SOL}\right), \quad H_{\infty,SOL} = R_g T_g / (k_G^{-1} k_G^0).$

shows that moderate changes may not destroy the overall calculation. Above 0.35–0.40 in rich loading, the simplified models start deviating significantly from the experimental values. Note that the penetration model still yields values reasonably similar to the experimental ones at these high loadings, showing the strong predictive tool this model represents. The SBDC model gives the best results of the simplified models but the improvement compared with the Hatta model is not that large. Table 2, columns 1–3, representing the Hatta number, the DeCoursey, and the SBDC models, respectively, gives a summary of the total AAD and AD of the interface models from the experimental data. It is clear that the penetration model offers the best agreement to the whole data set and in particular in the high loading range. The main reason why the enhancement factor based models fail before the penetration model is, in our opinion, their dependency on approximations of the infinite enhancement factor, in particular, at low driving forces where the enhancement factors become very large. The penetration model is designed to take into account the species and transport parameter profiles in the film, and has therefore better flexibility to cope also at high loading and with small driving forces. This is also reflected in the need for very high grid resolution in the penetration model in order to catch the very steep profiles in the free CO_2 concentration, whereas the enhancement models average over the film. For the enhancement factor models, the estimate of E_∞ based on Eq. 2 needs the concentrations of free amine and CO_2 in the bulk as well as at the interface. Possibly, an expression for the infinite enhancement factor using all of the species in the bulk solution might improve the performance of these models.

The need for a rigorous interface model at high loadings with a proper description of the diffusion mechanisms for reactants and products has previously been addressed by

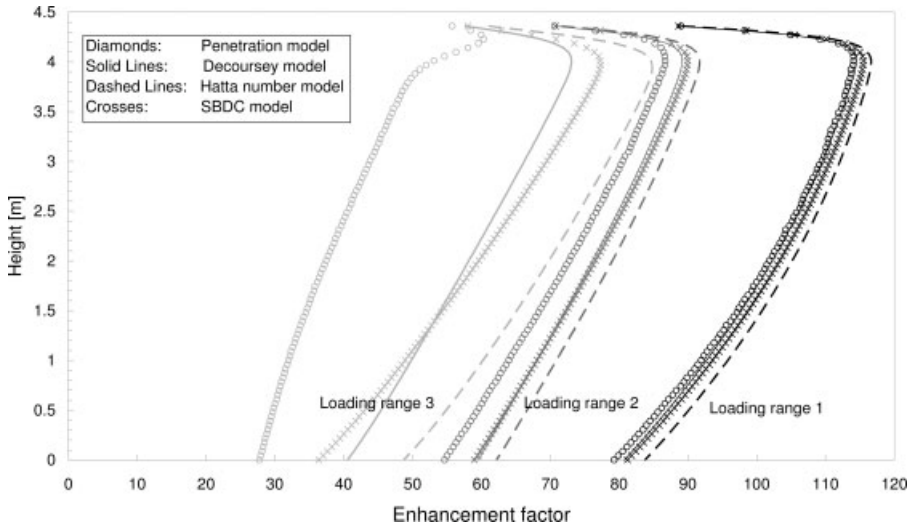

Figure 15. Penetration model (Pen., diamonds), DeCoursey (Dec., solid lines), Hatta number (*Ha*, dotted lines), and Secour–Buetler–DeCoursey (SBDC, dash-dotted lines) enhancement factors versus packing height. Loading ranges 1–3.

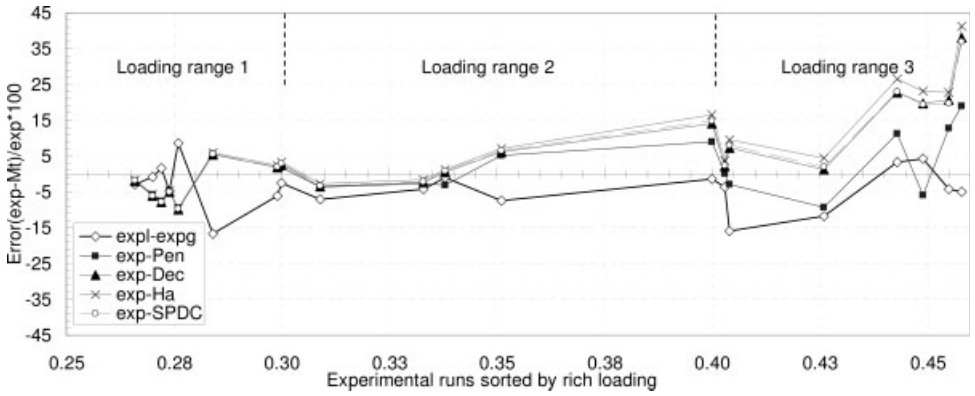

Figure 16. Experimental/simulation deviations for all pilot-plant test runs as function of rich loading for the different interface models.

Dang and Rochelle.[37] They observed large deviations from their model using a series resistance enhancement model which included pseudo first-order reaction and instantaneous reaction assumptions.

The numerical interface model as well as the enhancement models consider only the carbamate formation reaction and simple second order kinetics is assumed. Since the carbamate stability for MEA is high, the importance of a direct bicarbonate reaction is small and has been disregarded. However, at loadings around 0.5 the production of bicarbonate by reversion from carbamate can become significant. It is possible that this assumption could be a source for deviations in the high loading runs in range 3.

The effective interfacial area for mass transfer. The accuracy of the mass-transfer models depends to a large extent on the accuracy of the calculation of the effective interfacial area since this is directly proportional to the overall mass transfer in the packing. The available correlations from the literature considering the type of packing used in this work (Mellapak 250Y) show large variation in the estimated area values. Most of these models are semi-empirical and based on the falling film theory for laminar flow and inclined plates. The results of the calculations are to a large extent dependent on the absorber operating conditions and the geometric parameters to which the interface area model has been fitted. Several interfacial area models have been tested in this work and it was found that the most reasonable and consistent routine for Sulzer Mellapak 250Y was the one from De Brito et al.[27] A comparison of different routines showed that the correlation from Billet and Schultes[29] gave unreasonably low effective interfacial areas at high vapour velocities. De Brito et al.[27] report that for certain conditions, Mellapak 250Y can provide an effective mass-transfer area higher than the geometric area defined by the nominal packing surface.[27] The correlation from Brunazzi et al.[38] showed similar values as the correlation from De Brito et al., while the correlations obtained from Rocha et al.[25,26] yield slightly lower values. A summary of the applicable correlations found in the literature for Mellapak 250Y is shown in Table 6, together with interfacial area results for conditions encountered in our pilot unit.

Table 6. Calculated Effective Mass Transfer Areas for Sulzer Mellapak 250Y

Correlation	a_{ph} m^2/m^3	Comments
Brunazzi et al.	230–235	Explicit function of hold-up
Brovo and Rocha	207–200	Includes surface tension, not a function of hold-up
De Brito et al.	222–238	Not a function of hold-up

Experimental Run 1, percent vapor flood: 85, vapor velocity 2.5 m/s. Liquid hold-up estimated from correlation by Suess and Spiegel.[22]

As shown, the interfacial area is not predicted to change significantly along the packing. However, the correlations differ and this alone causes the total mean error for the dataset to change. The AAD, however, does not change to the same extent when one set of correlations is replaced by another. In other words, changing the correlation used for the effective interfacial area changes the degree of conformity of simulated results to the experimental results but not the precision of the data along the loading range.

Overview of model sensitivity to parameter changes. The presented model uses a large number of correlations obtained from laboratory scale experiments in which many assumptions have been made. These empirical correlations have built in uncertainties both with respect to the data they were based on, and also with respect to their applicability to the case at hand. To investigate the effects of these uncertainties, a sensitivity analysis was performed for some essential parameters and relations by increasing the base value by a certain percentage.

$$\%_{\text{dev}} = \frac{MT_{\text{Exp,liq}} - MT_{\text{sim}}^{3-20\%*}}{MT_{\text{Exp,liq}}} \times 100 \qquad (5)$$

Here * means a percentage change in the parameter tested. This percentage has been chosen such that it should cover an estimated uncertainty in the parameter.

The sensitivity analysis was performed for the following expressions and correlations:

(1) Using enhancement model where $E = Ha$,
(2) Using enhancement model of DeCoursey,[12]
(3) Using enhancement model of Hogendoorn et al.[15] (SBDC model),
(4) The reaction rate for CO_2 [15% change],
(5) Diffusivity of carbamate [15% change],

(6) Heat of absorption for CO_2 [15% change],
(7) Using effective area correlation from Brunazzi et al.,[38]
(8) Lumped parameter for contact time [20% change],
(9) Tuning of the equilibrium model 2–4% with respect to experimental data.

Tests 1–3, 7, and 9 are discussed earlier. Sensitivity tests 4–9 were all run with the penetration model as mass-transfer model. The analyses were performed with the aim of investigating the total CO_2 mass-transfer change. Table 2 shows the AAD and the AD for the whole data set, obtained when making the changes listed above. Generally it can be seen that the perturbations invoked yield very small changes in the final results, in this case shown by the ADD and AD. With the experimental accuracy of the tests the results are for all practical purposes the same. This implies that the sensitivity to errors in CO_2 reaction rate, carbamate diffusivity, heat of absorption, and contact time between mixing points is quite low. However, there is a tendency in the data set that the sensitivities increase with increasing loading.

Conclusions

Detailed experimental data from the absorber part of a 3-month campaign in a laboratory pilot plant capturing CO_2 with 30 wt % MEA were presented and used for a thorough validation of a rate based simulation model. The gas–liquid material balance in the experimental data was within an average of about 6%. The model was tested against all the obtained experimental data and the deviation between simulated and averaged gas and liquid side experimental mass-transfer rates yielded a total variability (AAD) of 6.26%, while the total AD was 6.16% which was deemed satisfactory. Also the agreement between experimental and simulated temperature profiles through the column was found to be satisfactory. Several enhancement factor models were tested and were shown to over-predict the mass-transfer rates at high loadings compared with the penetration model. Of the enhancement models tested, the SBDC and DeCoursey enhancement models gave the best results with an AAD and AD for the dataset of about 9%. A sensitivity analysis showed that the single most important source of deviation between experiments and model was the description of the equilibrium, in particular, at high loadings.

Acknowledgments

Financial support for this work by the Research Council of Norway Klimatek Programme through the SINTEF Project 661292 and by the European Commission through the CASTOR Integrated Project (Contract no. SES6-CT-2004-502856) is greatly appreciated. The authors also acknowledge the help of Dr. Karl Anders Hoff with the equilibrium model.

Notation

Definitions

a_{ph} = actual interfacial area of wetted packing (m^2/m^3)
d = diameter packing (m)
k_2 = forward reaction-rate coefficient
m = Henry distribution coefficient [−]
n = molar flow [kmol/(m^2 s)]
p_i = partial pressure of component i (kPa)
q = sensible heat flux (kJ/h)
y = molar fraction vapor phase
z = axial distance for packing (m)
A, B, C, D = main chemical components
D_i = Fick diffusion coefficent (m^2/s)
E = enhancement coefficient
F = flow rate (kmol/h)
H = specific enthalpy (kJ/kmol)
Ha = Hatta number
H_i = Henry coefficient of component i
K_{Eq,Co_2} = equilibrium constant for overall carbamate reaction (m^3/kmol)
N = interfacial molar flux [kmol/(m^2 s)]
P = pressure (kPa)
R = reaction-rate source term [kmol/(m^3 s)]
T = temperature (K) or (°C)
Z' = dimensionless axial distance

Subscripts

0 = at packing inlet
i = components undergoing mass transfer, or chemical reaction number
j = inert components
k = acid gas component
l,g = liquid, gas phase
w = weight fraction

Superscripts

− = time Average operator or for mixture liquid or gas
in = gas/liquid interface
b = bulk liquid
eq. and * = at equilibrium

Greek letters

γ = activity coefficient
Δ = dimensionless pressure
θ = dimensionless enthalpy
η = dimensionless molar flux, viscosity [kg/(m^{-1} s^{-1})]
ρ = density (kg/m^{-3})
ϕ = volume fraction
ν = stoichiometric coefficient
τ = characteristic contact time (s)

Literature Cited

1. Climate change 2001: the scientific basis. Third assessment report of the intergovernmental panel on climate change. Cambridge, United Kingdom: Cambridge University Press, 2001.
2. St. Clair JH, Simister WF. Process to recover CO_2 from flue gas gets first large scale tryout in Texas. *Oil Gas J*. 1983;6:109–113.
3. Reddy S, Roberts C. Fluor's Econamine FG Plus^{SM} technology: an enhanced amine-based CO_2 capture process. Presented at the Second National Conference on Carbon Sequestration, Alexandria, USA, May 5–8, 2003.
4. Tobiesen FA, Hoff KA, Svendsen HF. Desorber energy consumption in amine based absorption plants. *Int J Green Energy*. 2005;2:201–215.
5. Danckwerts PV, Alper E. Design of gas absorbers-3. Laboratory point model of a packed column absorber. *Trans Inst Chem Eng*. 1975;1:34–40.
6. De Leye L, Froment GF. Rigorous simulation and design of columns for gas absorption and chemical reaction-I. Packed columns. *Comput Chem Eng*. 1986;10:493–504.
7. Pandya JD. Adiabatic gas absorption and stripping with chemical reaction in packed towers. *Chem Eng Commun*. 1983;19:343–361.
8. Alatiqi L, Sabri MF, Bouharma W, Alper E. Steady-state rate-based modeling for CO_2/amine absorption–desorption. *Gas Sep Purif*. 1994;8:3–11.
9. Kucka L, Muller I, Kenig EY, Gorak A. On the modeling and simulation of sour gas absorption by aqueous amine solutions. *Chem Eng Sci*. 2003;58:3571–3578.

10. Al-Baghli NA, Pruess SA, Yesavage VF, Selim MS. A rate-based model for the design of gas absorbers for the removal of CO_2 and H_2S using aqueous solutions of MEA and DEA. *Fluid Phase Equil.* 2001;185:31–43.
11. Freguia S, Rochelle GT. Modeling of CO_2 capture by aqueous monoethanolamine. *AIChE J.* 2003;4:1676–1686.
12. DeCoursey WJ. Enhancement factors for gas absorption with reversible reaction. *Chem Eng Sci.* 1982;37:1483–1489.
13. Olander DR. Simultaneous mass transfer and equilibrium chemical reaction. *AIChE J.* 1960;6:233–239.
14. Weiland RH, Rawal M, Rice RG. Stripping of carbon dioxide from monoethanolamine solutions in a packed column. *AIChE J.* 1982; 28:963–972.
15. Hogendoorn JA, Vas Bhat RD, Kuipers JAM, van Swaaij WPM, Versteeg GF. Approximation for the enhancement factor applicable to reversible reactions of finite rate in chemically loaded solutions. *Chem Eng Sci.* 1997;52:4547–4559.
16. Bird RB, Steward WE, Lightfoot EN. *Transport Phenomena, 1st ed.* New York: Wiley, 1960.
17. Villadsen J, Michelsen ML. *Solution of Differential Equation Models by Polynomial Approximation.* Englewood Cliffs, NJ: Prentice-Hall, 1978.
18. Hoff KA. *Modeling and Experimental Study of Carbon Dioxide Absorption in a Membrane Contactor*, PhD Dissertation. NTNU, Norway, 2003.
19. Hoff KA, Juliussen O, Falk-Pedersen O, Svendsen HF. Modeling and experimental study of carbon dioxide absorption in aqueous alkanolamine solutions using a membrane contactor. *Ind Eng Chem Res.* 2004;43:4908–4921.
20. Ma'mun S, Nilsen R, Svendsen HF, Juliussen O. Solubility of carbon dioxide in 30 mass % monoethanolamine and 50 mass % methyldiethanolamine solutions. *J Chem Eng Data.* 2005;50:630–634.
21. Jou FY, Mather AE, Otto FD. The solubility of CO2 in a 30 mass percent monoethanolamine solution. *Can J Chem Eng.* 1995:73;140–147.
22. Liu Y, Zang L, Watanisiri S. Representing vapor–liquid equilibrium for an aqueous MEA-CO_2 system using the electrolyte nonrandom-two-liquid model. *Ind Eng Chem Res.* 1999;38:2080–2090.
23. Austgen DM, Rochelle GT, Chen CC. Model of vapor–liquid equilibria for aqueous acid gas-alkanolamine systems using the electrolyte-NRTL equation. *Ind Eng Chem Res.* 1989;28:1060–1073.
24. Poplsteinova J, Krane J, Svendsen HF. Liquid phase composition determinations in CO_2-H_2O-alkanolamine systems: an NMR study. *Ind Eng Chem Res.* 2005;44:9894–9903.
25. Rocha JA, Bravo JL, Fair JR. Distillation columns containing structured packings: a comprehensive model for their performance. I. Hydraulic models. *Ind Eng Chem Res.* 1993;32:641–651.
26. Rocha JA, Bravo JL, Fair JR. Distillation columns containing structured packings: A comprehensive model for their performance. II. Mass-transfer model. *Ind Eng Chem Res.* 1996;35:1660–1667.
27. De Brito MH, von Stockar U, Bangerter AM, Bomio P, Laso M. Effective mass-transfer area in a pilot plant column equipped with structured packings and with ceramic rings. *Ind Eng Chem Res.* 1994;33:647–656.
28. Suess P, Spiegel L. Hold-up of Mellapak structured packings. *Chem Eng Proc.* 1992;31:119–124.
29. Billett R, Schultes M. Prediction of mass transfer columns with dumped and arranged packings. *Trans Inst Chem Eng A.* 1999;77: 498–504.
30. Wilson GM. Vapour–liquid equilibrium. XI. A new expression for the excess free energy of mixing. *J Am Chem Soc.* 1964;86:127–130.
31. Nath A, Bender E. Isothermal vapor–liquid equilibria of binary and ternary mixtures containing alcohol, alkanolamine, and water with a new static device. *J Chem Eng Data.* 1983;28:370–375.
32. Irvine TF, Liley PE. *Steam and Gas Tables with Computer Equations.* San diego, CA: Academic press, 1984.
33. Versteeg GF, van Dijck LAJ, van Swaaij WPM. On the kinetics between CO_2 and alkanolamines both in aqueous and non-aqueous solution: an overview. *Chem Eng Commun.* 1996;144:113–158.
34. Mathonat C, Majer V, Mather AE, Grolier J-PE. Enthalpies of absorption and solubility of CO_2 in aqueous solutions of methyldiethanolamine. *Fluid Phase Equil.* 1997;140:171–182.
35. Dugas RE, Rochelle GT, Seibert F. CO_2 capture performance of a monoethanoloamine pilot plant. In Proceedings of the 8th International Conference on Greenhouse Gas Control Technologies (GHGT-8), Trondheim, Norway, 2006.
36. Aboudheir A, Tontiwachwuthikul P, Chakma A, Idem R. Kinetics of the reactive absorption of carbon dioxide in high CO_2-loaded, concentrated aqueous monoethanolamine solutions. *Chem Eng Sci.* 2003;58:5195–5210.
37. Dang H, Rochelle G. CO_2 absorption rate and solubility in monoethanolamine/piperazine/water. *Sep Sci Tech.* 2003;2:337–357.
38. Brunazzi E, Nardini G, Paglianti A, Petarca L. Interfacial Area of Mellapak packing: absorption of 1,1,1-Trichloroethane by Gensorb 300. *Chem Eng Technol.* 1995;18:248–255.
39. Hoogendoorn GC, Abellon RD, Essens PJM, Wesselingh JA. Desorption of volatile electrolytes in a tray column. *Chem Eng Res Des.* 1988;66:483–502.
40. Blom JG, Zegeling PA. Algorithm 731: a moving-grid interface for systems of one-dimensional time-dependent partial differential equations. *ACM Trans Math Softw.* 1994;20:194–214.
41. Petzold L. A description of DASSL: a differential-algebraic equation solver. In Proceedings of the 10th IMACS World Congress, Montreal, Canada, 1982.
42. Tamimi A, Rinker EB, Sandall O. Diffusion Coefficients for Hydrogen Sulfide, Carbon Dioxide, and Nitrous Oxide in water over the Temperature range 293–368 K. *J Chem Eng Data.* 1994;39:330–332.
43. RC, Prausnitz JM, Poling BE. The properties of gases and liquids (4th edition). New York: McGraw-Hill Book Co., 1986.
44. Weiland RH, Dingman JC, Cronin DB, Browning GJ. Density and viscosity of some partially loaded carbonated aqueous alkanolamine solutions and their blends. *J Chem Eng Data.* 1998;43:378–382.
45. Cheng S, Meisen A, Chakma A. Predict amine solution properties accurately. *Hydrocarb Process.* 1996;2:81–84.
46. Zquez G, Alvarez E, Navaza JM, Rendo R, Romero E. Surface tension of Binary Mixtures of Water + Monoethanolamine and Water + 2-Amino-methyl-1-propanol and Tertiary Mixtures of these Amines with Water from 25°C to 50°C. *J Chem Eng Data.* 1997:42: 57–59.

Appendix A: Model Equations for Packing

Mathematical description of flow model for packing

In order to obtain a mathematical model describing the mass transfer with simultaneous chemical reaction in a differential absorber, the following assumptions were made regarding the flow model:

- Axial dispersion is small in comparison with the convective flux. Thus, in this work, backmixing is disregarded. For industrial packed-bed reactors, the flow fields are highly turbulent in both phases. It is therefore reasonable to assume that there are also negligible radial gradients in temperature and concentration along the tower. The flow fields for both the liquid and vapor phases are, based on this, considered to be plug flow.
- Vapor in the gas phase condenses at the gas–liquid interface, releasing heat of condensation instantaneously to the liquid phase.
- All chemical reactions are restricted to the liquid phase.
- The packed section has one liquid and one gas feed stream.
- The packed section has one liquid and one gas exit stream.
- The heat loss to the surrounding is disregarded since the pilot absorber was insulated and assumed adiabatic.
- The transferring components leave and enter the gas phase at the gas phase temperature.

For a steady-state 1-D model disregarding effects of axial and radial dispersion in both phases, the general continuity

equations reduces to the following where positive is defined as along the direction of flow for both phases:

Vapor phase transport equations

The molar transfer rates for a component flowing as plug flow through the column may be written as:

$$-\frac{dn_{g,i}}{dz} = N_i a_{ph} \tag{A1}$$

where subscript i refers to the gas phase components undergoing mass transfer.

All other components that do not undergo interfacial transfer, e.g. inerts, are carried through the column, $-\frac{dn_{g,j}}{dz} = 0$.

Heat balance:

$$-\frac{d(\sum(n_{g,i}H_{g,i}))}{dz} = \left(\sum(N_i H_{g,i}) + q_g\right)a_{ph} \tag{A2}$$

Liquid phase transport equations

Component molar balance:

$$-\frac{dn_{l,i}}{dz} = N_i a_{ph} \tag{A3}$$

where subscript i refers to the components in the liquid phase undergoing mass transfer.

Heat balance:

$$-\frac{d(\sum(n_{l,i}H_{l,i}(T_l)))}{dz} = \left(\sum(N_i H_{g,i}(T_g)) + q_g\right)a_{ph} + \frac{4}{d_r}q_w \tag{A4}$$

Pressure drop:

$$-\frac{dP_{tot}}{dz} = f(\ldots) \tag{A5}$$

where $f(\ldots)$ is a pressure drop correlation. In this validation paper, it is assumed that the pressure drop is linear from the measured inlet to the outlet pressure.

The boundary conditions for this type of steady-state BVP are given by:

$$\begin{aligned} &\text{Gas phase:} \quad \text{At } z = 0: \quad n_{g,i} = n_{g,i,0} \quad \text{and} \quad T_g = T_{g,0} \\ &\text{Liquid phase:} \quad \text{At } z = L: \quad n_{l,i} = n_{l,i,0} \quad \text{and} \quad T_l = T_{l,0} \end{aligned}$$

The equations are made dimensionless:

$$\theta_g = \frac{n_{g,i}H_{g,i}}{\sum_i(n^0_{g,i}H^0_{g,i})}, \quad \theta_l = \frac{n_{l,i}H_{l,i}}{\sum_i(n^0_{l,i}H^0_{l,i})}, \quad \Delta = \frac{P}{P^0}$$

$$\eta_{g,i} = \frac{n_{g,i}}{\sum_i n^0_{g,i}}, \quad \eta_{l,i} = \frac{n_{l,i}}{\sum_i n^0_{l,i}}, \quad Z' = \frac{z}{L}$$

To obtain the following dimensionless equations:

Normalized gas phase equations

Mass:

$$-\frac{d\eta_{g,i}}{dZ} = \frac{L}{\sum_i n^0_{g,i}} \times N_i a_{ph} \tag{A6}$$

Enthalpy:

$$-\frac{d(\sum(\eta_{g,i}H_{g,i}))}{dZ} = \frac{L}{\sum_i(n^0_{g,i}H^0_{g,i})} \times \left(\sum(N_i H_{g,i}) + q_g\right)a_{ph} \tag{A7}$$

Normalized liquid phase equations

Mass:

$$-\frac{d\eta_{l,i}}{dZ'} = \frac{L}{\sum_i n^0_{l,i}} \times N_i a \tag{A8}$$

Enthalpy:

$$-\frac{d(\sum(\eta_{l,i}H_{l,i}(T_l)))}{dZ} = \frac{L}{\sum_i(n^0_{l,i}H^0_{l,i})} \times \left(\left(\sum(N_i H_{g,i}(T_g)) + q_g\right)a_{ph} + \frac{4}{d_r}q_w\right) \tag{A9}$$

Pressure drop relation

$$\frac{d\Delta}{dZ'} = \frac{L}{P^0}f(\ldots) \tag{A10}$$

Appendix B: Gas/Liquid Interface Model Equations

Penetration model: assumptions

- The model contains one parameter, the contact time, in which all the details of the real fluid dynamics are lumped. The gas/liquid contact between the mixing points is calculated using an empirical correlation based on the packing hydraulics.[26]
- The bulk of both phases are assumed to be well mixed.
- The system is dilute with respect to the transferring component and diffusion-induced convection can be neglected. Therefore the total molar flux is equal to the diffusion flux.
- Temperature gradients in the mass-transfer film are disregarded.

Problem Formulation. Mass transfer with chemical reaction of general order with respect to both reactants and products:

$$A(g) + v_b B(l) \leftrightarrows v_c C(l) + v_d D(l) \tag{B1}$$

For the overall reaction with MEA: B = MEA, C = $MEAH^+$, D = $MEACOO^-$, $v_b = 2$, and $v_c = v_d = 1$.

The rate equation uses second-order kinetics for a reversible overall reaction (see Appendix B2). The rate expression is used

in the source term in the mass balances for each node and for each species. For the reactant (MEA): $R_b = \nu_b R_k$ and reaction products, protonated amine and carbamate: $R_{c,d} = -\nu_{c,d} R_k$.

The equation describing the mass balance for each component:

$$\frac{\partial \overline{C}_i}{\partial t} = \frac{\partial}{\partial x}\left(\overline{D}_i \frac{\partial \overline{C}_i}{\partial x}\right) - \nu_i R_k \tag{B2}$$

For each of the four chemical species considered there is one nonlinear partial differential equation of parabolic type. These can become very stiff depending on the reaction term. Fick's law is used to represent diffusional fluxes assuming pseudo-binary diffusion. The bulk equilibrium concentrations of all species participating in the chemical reactions are needed for the initial condition and can be obtained from the equilibrium model.

Initial conditions and boundary conditions. IC:

At $t = 0$ and $x \geq 0$:

$$C_i = C_i^{b,eq.} \tag{B3}$$

BC:

At $t = 0$ and $x = 0$:

The transferring components:

$$-D_k \left.\frac{dC_k}{dx}\right|_{x=0} = k_g\left(\frac{\phi_k P_k^b}{RT_g} - \frac{\gamma_k H_k^{in} C_k^{in}}{RT_g}\right) \tag{B4}$$

For nontransferring components:

$$-D_i \left.\frac{dC_i}{dx}\right|_{x=0} = 0 \tag{B5}$$

At $t > 0$ and $x = 1$:

$$C_i = C_i^{b,eq.} \tag{B6}$$

Here ϕ_k is the fugacity coefficient of the k (acid gas) component which takes the nonideality of the gas phase into account. The fugacity coefficient has been found to not differ more than 1–2% from unity for a pressure less than 0.2 MPa.[39] It was therefore assumed to be unity.

The total time-averaged CO_2 flux can then be calculated:

$$\overline{N}_k = \left(\frac{1}{\tau}\right)\int_0^{\delta} (C_{i'}^{j} - C_{i'}^{b,eq.}) d\delta = Ek_{L,k}^0(\gamma_k^{ln} C_k^{in} - \gamma_k^{b,eq.} C_k^{b,eq.}) \tag{B7}$$

where i' indicates all liquid species containing acid gas, free and chemically bound, and indicates all species in the solution other than the acid gas component k. The enhancement factor, defined from this equation, can easily be calculated for comparisons with the asymptotic cases since the flux is calculated directly.

After normalizing the equations to dimensionless terms, the initial value problem (IVP) is solved using the method of lines (MOL). This is a general technique for solving partial differential equations (PDEs). Since the gradients at the interface become extremely steep, there must be a large number of grid points located close to the interface in order to correctly capture the gradients. On the other hand, the time needed to solve the set of PDEs increases with the number of grid points. This occurs because the PDEs need to be solved at each grid point, and there is one call to the equilibrium model per grid point. The problem is therefore solved using an adaptive moving grid[40] in the space direction to yield a set of ordinary differential equations that is solved by an appropriate stiff time-integrator. This approach requires an interpolation of variables whenever the location of grid points change. In this work, the integration package DASSL is used.[41] To obtain a similar quality of solution, using a static grid, at least four times as many grid points must be used. This method has shown to be fast and accurate for obtaining the interfacial flux when applying the penetration model.

Kinetics: assumptions around the set of chemical reactions in the liquid film

Kinetically controlled reversible reactions:

Overall reaction for CO_2 and a primary amine RHNH:

$$CO_2 + 2RNNH \leftrightarrows RHNCOO^- + RHNH_2^+ \tag{B8}$$

$$CO_2 + OH^- \leftrightarrows HCO_3^- \tag{B9}$$

$$CO_2 + H_2O \leftrightarrows H_2CO_3 \tag{B10}$$

Instantaneous reversible reactions:

$$2H_2O \leftrightarrows H_3O^+ + OH^- \tag{B11}$$

$$HCO_3^- + H_2O \leftrightarrows + H_3O^+ + CO_3^{2-} \tag{B12}$$

$$RHNH_2^+ + H_2O \leftrightarrows H_3O^+ + RHNH \tag{B13}$$

The carbamate reversion:

$$RHNCOO^- + H_2O \leftrightarrows HCO_3^- + RHNH \tag{B14}$$

Bicarbonate formation by reactions B9 and B14 and carbonate formation by reaction B12 are not considered in the kinetic model, and transport equations for these species are not included. However, they are taken into account in the equilibrium model both in bulk and reaction zone. The chemical equilibrium constants used for this system were obtained from Austgen et al.[23] as functions of temperature at "infinite dilute concentrations." The forward reaction constant is taken from Versteeg et al.[33] It is assumed that the reactions with MEA and CO_2 involve second-order kinetics, first order in both CO_2 and MEA. This is found experimentally for MEA.[33]

The rate term can then be expressed as:

$$R_a = k_2 c_A c_B^{\nu_b} - k_{-2} c_c^{\nu_c} c_d^{\nu_d} \tag{B15}$$

which rearranges to

$$R_a = k_2\left(c_a c_b^{\nu_b} - \frac{1}{K_{eq}} c_c^{\nu_c} c_d^{\nu_d}\right) \tag{B16}$$

It is common to substitute the back-reaction concentrations with the forward concentrations being in equilibrium with them:

$$R_a = k_2(c_a^j c_b^{j,\nu_b} - c_a^{j,*} c_b^{j,\nu_b *}) \tag{B17}$$

We have used a model where activity coefficients are included for CO_2:

$$R_a = k_2(\gamma_k^j c_k^j (c_b^j)^{\nu_b} - \gamma_k^{j,*} c_k^{j,*} (c_b^{j,*})^{\nu_b}) \tag{B18}$$

When the penetration model is used, j indicates the location in the discretized film and k is the acid gas component. When the enhancement factor model is used, the driving force is based on the difference between the interface activity and the bulk liquid activity. This expression is used in the source term in the discretized mass balance equations at each node j and for each of the four species. The driving force is thus based on activities for CO_2 while it is based on concentration for the other species. The kinetic expression in Eq. B16, including activity coefficients for CO_2, was also tested and gave negligible changes to the results.

Appendix C: Correlations and Functions Used in the Model

Table C1. Overview of Correlations Implemented in the Computer Code

Parameter/Correlation	Comment	Reference
$k_{G,0}$	For all transferring components	Bravo et al. (1996)[26]
$k_{L,0}$	For CO_2 liquid phase using enhancement model only	Bravo et al. (1996)[26]
τ (contact time)	For CO_2 liquid phasse penetration model only	Bravo et al. (1996)[26]
Liquid hold-up	For $k_{L,0}$, a_{ph}	De Brito et al. (1996)[27]
a_{ph} (eff. interfacial area)	For all transferring components	Bravo et al. (1993)[25]
Flooding velocities, liquid, and vapor	Used to estimate size of tower	Billet and Schultes (1999)[29]

Table C2. Overview of Functions Implemented in the Computer Code

Parameter	Phase	Functions	Reference/Comment
Diffusion coefficients	Liquid:Reactants	T_L, viscosity, x_i	Versteeg et al. (1996)[33] and Tamini et al. (1994)[42]
	Liquid:Products	T_L, viscosity, x_i	Hoff et al. (2003)[18]
	Vapor		Methode of Fuller, Reid et al. (1986)[43]
Viscosity	Liquid	T_L, x_i	Weiland et al. (1998)[44]
	Vapor	T_L, y_i	Methode of Wilke, Reid et al. (1986)[43]
Desity	Liquid	T_L, w_i, CO_2 added as a weighed addition	Cheng et al. (1996)[45]
	Vapor	T_G, y_i	Reid et al. (1986)[43]
Enthalpy	Vapor	T_G, y_i	Reid et al. (1986)[43]
	Liquid	T_L, w_i	Cheng et al. (1996)[45]
Surface tension	Liquid		Vázquez et al. (1997)[46]
Heat of reaction CO_2	Liquid	T_L, x_i	Aboudheir et al. (2003)[36] and own data.
Heat of vapor MEA	Liquid	T_L, x_i	Difference between H_g and H_l
Heat of vapor H_2O	Liquid	T_L, x_i	Difference between H_g and H_l
Activity coefficients	Vapor: H_2O, MEA	T_L, x_i, P	Nath and Bender (1983)[31]
Henry parameter CO_2		T_l, x_i	Austgen et al. (1989)[23]

Appendix D: Stream Enthalpy Calculations

Specific liquid enthalpy for streams:

$$\overline{H}_l(T_l,x_i) = \left(\sum_i x_i H^0_{l,\mathrm{ref},i}\right) + \left[\sum_i (x_i m w_i)\int_{T_{\mathrm{ref}}}^{T_l} Cp(T,w_i)_{\mathrm{mix}}\,dT\right] + x_k\left[H^0_{g,\mathrm{ref},k} + \int_{T_{\mathrm{ref}}}^{T_l} Cp(T)_{g,k}\,dT\right] + x_{Am}\int_{y_{\mathrm{ref}}}^{y_l} (-\Delta H_{Abs}(y_k,T_l))\,dy \tag{D1}$$

Specific vapor enthalpy for streams:

$$\overline{H}_g(T_g) = \sum_i \left(y_i\left[H^0_{g,\mathrm{ref},i} + \int_{T_{\mathrm{ref}}}^{T_g} Cp(T)_{g,i,\mathrm{ideal}}\,dT\right]\right) \tag{D2}$$

Appendix E: Pilot Rig Measured Data

Table E1. Feed Gas Phase

Vapor Run*	Flow Rate, wet (m^3/h)	T in (°C)	P in (kPa)	CO_2 in dry (vol %)	T out (°C)	P out (kPa)	CO_2 out, dry (vol %)
1	150	39	102.94	1.65	42.24	101.78	0.40
2	150	40	102.99	1.57	41.86	101.78	0.35
3	151	39	102.99	1.56	41.35	101.78	0.36
4	151	40	102.99	1.57	41.74	101.79	0.35
5	150	54	100.38	2.04	53.41	99.30	0.39
6	150	54	102.17	2.41	55.60	101.09	0.34
7	150	52	101.80	3.03	53.40	100.29	0.86
8	148	50	102.04	2.41	52.00	100.34	0.47
9	152	62	101.47	3.19	64.70	100.28	0.67
10	151	54	101.17	2.81	58.00	100.16	0.64
11	151	53	101.24	2.16	55.80	100.21	0.45
12	151	51	101.83	2.96	54.40	100.78	1.29
13	151	64	101.97	6.65	68.40	100.80	3.04
14	153	51	103.05	4.34	53.80	101.94	3.13
15	143	62	103.38	12.12	66.60	100.98	8.13
16	151	60	103.96	9.44	62.88	102.73	7.93
17	144	68	103.06	15.33	68.52	101.36	13.00
18	151	69	103.80	12.50	72.43	100.84	7.08
19	142	66	102.11	8.35	70.49	100.34	4.51
20	142	64	102.14	4.54	68.79	100.37	1.52

*Sorted by date.

Table E2. Feed Liquid Phase

Liquid Run*	Flow Rate (l/min)	T in (°C)	Inlet CO_2 Loading (mol/mol)	Inlet Density (kg/m^3)	T out (°C)	Outlet CO_2 Loading (mol/mol)	Outlet Density (kg/m^3)	Conc. MEA, 25°C ($kmol/m^3$)	$T4$ max** (°C)
1	4	40	0.218	1060	41	0.284	1069	4.91	48.5
2	4	41	0.220	1056	42	0.275	1073	4.91	48.4
3	4	40	0.215	1061	41	0.272	1069	4.91	48.1
4	4	41	0.217	1058	42	0.276	1070	4.91	48.4
5	4	51	0.216	1059	55	0.274	1075	4.91	58.9
6	4	50	0.183	1056	56	0.267	1072	4.93	60.8
7	6	49	0.284	1069	53	0.345	1081	4.63	60.0
8	6	48	0.241	1062	52	0.296	1072	4.74	58.7
9	6	61	0.233	1059	64	0.299	1073	4.71	68.1
10	3	48	0.217	1058	56	0.333	1084	4.97	60.6
11	3	48	0.219	1059	54	0.309	1078	4.93	58.2
12	3	46	0.307	1080	52	0.401	1099	4.99	56.8
13	6	60	0.297	1080	66	0.390	1097	5.05	71.2
14	3	48	0.370	1092	52	0.443	1106	5.06	55.0
15	9	59	0.357	1090	64	0.435	1105	5.10	71.1
16	6.2	61	0.402	1100	61	0.447	1110	5.10	63.9
17	9	66	0.409	1102	67	0.451	1112	5.09	69.6
18	9	62	0.346	1090	69	0.429	1110	5.13	74.5
19	9	64	0.347	1088	68	0.400	1100	5.17	73.0
20	9	64	0.292	1084	67	0.339	1090	5.22	71.4

*Sorted by date.
**Temperature measurement in packing 3.3 m from packing bottom.

Manuscript received Mar. 24, 2006, and revision received Jan. 17, 2007.